European Biophysics Journal
https://doi.org/10.1007/s00249-018-1319-x

ORIGINAL ARTICLE

AUC measurements of diffusion coefficients of monoclonal antibodies in the presence of human serum proteins

Robert T. Wright[1] · David Hayes[2] · Peter J. Sherwood[3] · Walter F. Stafford[4] · John J. Correia[1]

Received: 12 January 2018 / Revised: 7 May 2018 / Accepted: 4 July 2018

Abstract
The goal of this work is to develop a preclinical method for quantitative hydrodynamic and thermodynamic analysis of therapeutic proteins in crowded environments like human serum. The method utilizes tracer amounts of fluorescently labeled monoclonal antibodies and the Aviv AU-FDS optical system. We have performed sedimentation velocity experiments as a function of mAb, human serum albumin and human IgG concentration to extract self- and cross-term hydrodynamic nonideality effects. SV measurements are consistently complicated by weak mAb–mAb and mAb–IgG interactions (Wright et al. in Anal Biochem 550:72–83, 2018). In an attempt to explore different approaches we have investigated measurements of diffusion coefficients by traditional synthetic boundary experiments. Here we present a new technique incorporated into SEDANAL that can globally analyze the full time course of synthetic boundary experiments. This approach also utilizes F-mAb against a high concentration of unlabeled carrier protein (HSA or IgG). In principle both diffusion and sedimentation coefficient information can be extracted including hydrodynamic and thermodynamic nonideality. The method can be performed at a traditional low speed (5–7K rpm) or at high speeds. The high speed method can also be used to measure D and s for small molecules like fluorescein (often contaminants of F-HSA and F-mAb). The advantage of synthetic boundary over the standard sedimentation velocity method is that it allows for higher precision determination of diffusion coefficients. The concentration dependence of D can be corrected for hydrodynamic nonideality effects by plotting $D^*(1+k_{ij}c_j)$ vs total carrier concentration. The slope of the fitted data allows an alternate approach to determine self- and cross-term thermodynamic nonideality. This method can also explore cross-term diffusion coefficient effects. These results are compared to dynamic light scattering approaches which are limited to k_D determinations for solutions of pure protein.

Keywords Second virial coefficient · Diffusion · Hydrodynamic nonideality · Sedimentation velocity · Synthetic boundary · Thermodynamic nonideality

Introduction

Sedimentation velocity has been useful for the analysis of weak macromolecular repulsive interactions for 70 years. The approach has been used to measure the concentration dependence of sedimentation k_s and diffusion k_D. The measurement of k_s from sedimentation velocity (SV) experiments is straight forward and has been implemented by many investigators utilizing different optical systems (Kegeles and Gutter 1951; Harrington and Schachman 1953; Schachman and Harrington 1954; Hersh and Schachman 1955, 1958; Harding and Johnson1985a, b; Solovyova et al. 2001; Saluja et al. 2010; Yadav et al. 2011; Correia et al. 2016; Wright et al. 2018). The measurement of k_D has been commonly performed by orthogonal methods like dynamic light scattering (DLS; Solovyova et al. 2001; Saluja et al. 2010). Determination of the second virial coefficient B can then be performed by application of a difference equation $k_D = 2BM - k^*$ that reveals that k_D comprises both hydrodynamic and thermodynamic contributions, and k^* is derived from a linear plot of s vs c (see "Discussion"; Harding and Johnson 1985a; Saluja

Special Issue: 23rd International AUC Workshop and Symposium.

✉ John J. Correia
jcorreia@umc.edu

[1] Department of Biochemistry, University of Mississippi Medical Center, Jackson, MS 39216, USA

[2] Boehringer-Ingelheim, Ridgefield, CT 06877, USA

[3] Interactive Technology, Oakland, CA 94602, USA

[4] Department of Systems Biology, Harvard Medical School, Boston, MA 02115, USA

Published online: 12 July 2018

et al. 2010). Since the sedimentation of a macromolecule also is influenced by both hydrodynamic (k_s) and thermodynamic (2BM) nonideality, it should in principle be possible to extract both parameters directly from SV data analysis alone (Solovyova et al. 2001; Wright et al. 2018). This can be seen in the following empirical expressions for concentration dependence and nonideality (Stafford and Sherwood 2004).

$$s = \frac{s^0}{1 + k_s c} \quad \text{and} \quad D = \frac{D^o(1 + 2BMc)}{(1 + k_s c)} \qquad (1 \text{ and } 2)$$

When expressed in this way, both k_s and $2BM$ can in principle be determined by global direct boundary fitting of SV data collected over a range of concentrations by the sedimentation analysis program SEDANAL (Stafford and Sherwood 2004). Recent studies on monoclonal antibodies in serum proteins (Correia et al. 2016; Wright et al. 2018; Yang et al. 2018) have attempted to implement this approach and have found that weak association reduces or masks k_s values. This means both nonideality and self-association are present in the solution and the result is typically a reduced apparent k_s value or a reduced apparent weak association. In addition, in the presence of a weak association, $2BM$ values are often negligible, the best fit goes to zero, and becomes difficult to determine by SV. This is thought to be due to the combination of thermodynamic nonideality and weak association effects on boundary shape. As the equation for D above shows, increases in $2BM$ cause boundary spreading while increases in k_s cause boundary sharpening, and thus offset one another. Thus, there appears to be a need for alternative ways of estimating $2BM$ from AUC methods.

Sedimentation velocity is usually performed at high speed under conditions where s is readily determined, but diffusion may be minimal for large macromolecules. Here we demonstrate that synthetic boundary (SB) experiments are amenable to determining s and D through direct boundary fitting with SEDANAL. When performed as a function of concentration this allows the extraction of $2BM$ values from the slope of plots of $D_{app}(1 + k_s c)$ vs c. When implemented with the Aviv Fluorescence Detection System (AU-FDS; Macgregor et al. 2004; Kroe and Laue 2009; Lyons et al. 2013) methods, this approach can also measure cross-term virial coefficient effects, B_{ij}, or the thermodynamic nonideality of mAbs in the presence of serum proteins. This method is appropriate for repulsive (positive BM) or attractive (negative BM) interactions and has proven useful in verifying the weak association of mAbs (Solovyova et al. 2001; Saluja et al. 2010; Yadav et al. 2011, 2012). Here we present detailed methods for AUC Aviv-FDS synthetic boundary measurements and their application to the determination of monoclonal antibody diffusion coefficients in the presence of high concentrations of serum proteins human serum albumin (HSA) and human IgG. The result is self- and cross-term $2B_{ij}M_j$ values that can verify thermodynamic nonideality or the presence of weak association.

Materials and methods

Samples

The NIST mAb and golimumab therapeutic IgG antibodies (100 mg/ml) were provided by Boehringer-Ingelheim. The second lot of golimumab (100 mg/ml) was also purchased from the University of Mississippi Medical Center pharmacy. Human serum albumin was purchased from Sigma-Aldrich in the fatty-acid free form (A3782). A heterogeneous mixture of the total human IgG serum fraction was obtained from Golden West Biologicals, Inc., Temecula, CA (HGG1000). Analytical ultracentrifugation experiments were run in phosphate-buffered saline (PBS; 150 mM NaCl, 2.7 mM KCl, 20 mM Na_2HPO_4, and 1.8 mM KH_2PO_4, pH 7.4). HSA, IgG and mAbs were stored as stock solutions dialyzed into PBS using Slide-A-Lyzer MINI Dialysis devices (Thermo Scientific).

Protein labeling

NIST mAb and golimumab were labeled with Alexa-Fluor 488 carboxylic acid, succinimidyl ester (Molecular Probes A20100). HSA was labeled with fluorescein 5(6)-isothiocyanate (Sigma-Aldrich F3651). Thermo Scientific (Alexa-Fluor 488) and Sigma fluorescein 5(6)-isothiocyanate (FITC) protocols for fluorescence labeling were followed. Typically 3–4 Alexa-488 molecules covalently bound per mAb, and ~0.5 FITC bound per HSA. Each labeled protein was run pair-wise in tracer level amounts with unlabeled carrier protein.

Analytical ultracentrifugation

All experiments were performed in a Beckman Coulter Optima XL-A analytical ultracentrifuge equipped with an Aviv AU-FDS fluorescence optical system at 20 °C. Samples were made up at the desired concentration (100–200 nM tracer and a range of unlabeled carrier concentrations) and loaded into double sector, 3 mm pathlength synthetic boundary cells (40 µl on sample side; Spin Analytical Spin50-SB-3 mm; Fig. 1). FC-43 (a fluorocarbon oil from Beckman, 20 µl) was introduced to the centerpiece in advance of the sample to remove the base of the sample from the optical artifact due to cut-off of the cone of FDS laser light. The centrifuge cells were placed into an An-60 Ti rotor and the temperature of the AUC was equilibrated for at least 1 h before the run began. Low speed runs were performed at

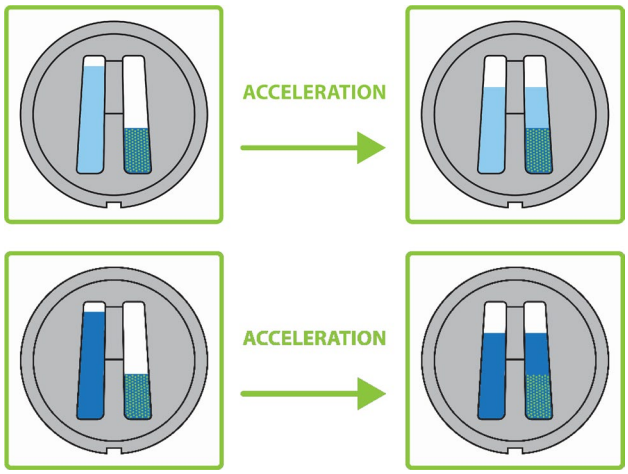

Fig. 1 Synthetic boundary centerpiece. Upon acceleration, buffer or solvent from the left sector flows via the etched channel onto the protein solution in the right sector creating a sharp boundary for observing diffusion and sedimentation. The upper panel shows gradient mode: buffer (light blue) layering onto labeled tracer (yellow) plus carrier protein (dark blue). The lower panel shows constant background or CB mode: carrier protein layering onto labeled tracer (yellow) plus carrier protein (dark blue)

7K rpm. High speed experiments were done at 35K rpm for HSA, 24K rpm for mAbs, and 50K rpm for small compounds like fluorescein. These higher speeds are chosen to give a reduced molecular weight, $\sigma = \frac{M_B \omega^2}{RT}$, of approximately 10 and provide optimal chance to estimate both s and D. Sedimentation was monitored by measuring absorbance at 280 nm for unlabeled protein samples, 492 nm for fluorescein, and by FDS for fluorescently labeled samples. Attempts to measure labeled protein sample via absorbance by the label (~488 nm) in high concentration carrier protein backgrounds failed due to the presence of significant Schlieren effects caused by the carrier protein gradient deflecting light out of the optical tract (Colfen and Harding, 1995; Dhami et al. 1995).

The density of PBS was measured in an Anton Paar DMA 5000 density meter. The buffer viscosity was estimated with Sednterp (Laue et al. 1992; Hayes et al. 1994). The partial specific volume (v_{bar}) was calculated from sequence information if available. For HSA, the concentration of the unlabeled component ranged from 1 to 40 mg/ml. Measurements on IgG runs ranged from 1 to 20 mg/ml. The experiments involving the unlabeled therapeutic antibody as the background molecule varied from 1 to 20 mg/ml. These ranges were chosen because typical serum has 30–35 mg/ml HSA and 12–15 mg/ml IgG. SEDANAL internally uses concentration units of mg/ml and thus k_s and $2BM$ have units of ml/mg to make $k_s c$ or $2BMc$ dimensionless (Eqs. 1 and 2). However, the field tends to use ml/g (Rowe 1977; Harding and Johnson 1985a, b; Solovyova et al. 2001; Saluja et al. 2010; Yadav et al. 2011) and thus we plot data vs mg/ml, but report data in units of ml/g. This also avoids reporting numbers with lots of digits (0.0033 ml/mg vs 3.3 ml/g). Carrier protein concentrations were estimated from absorbance measurements on dilutions of stock solutions with extinction coefficients based upon amino sequence as estimated by the program Sednterp (Laue et al. 1992): NIST $\varepsilon_{280} = 1.44$ ml/mg/cm; golimumab $\varepsilon_{280} = 1.49$ ml/mg/cm; HSA $\varepsilon_{280} = 0.52$ ml/mg/cm. For total IgG, the extinction coefficient is provided by the vendor: $\varepsilon_{280} = 1.36$ ml/mg/cm. The fluorescein extinction coefficient is taken from the Molecular Probes web site: $\varepsilon_{238\,nm} = 39{,}800\ M^{-1}$. Fluorescein SB experiments were performed with 150 nM by FDS or 35 µM by $Abs_{485\,nm}$ at both 7k and 50k rpm. Sedimentation and diffusion coefficient data were extrapolated to infinite dilution and corrected to $s^o_{20,w}$ and $D^o_{20,w}$. For presentation purposes carrier protein concentrations are plotted as mg/ml to match the phenomenological form of the concentration dependence (Eqs. 1 and 2). Tracer and fluorescein concentrations are listed as nM or µM to reflect the optical limitations of the AU-FDS system (Lyons et al. 2013).

SB experiments are traditionally done by layering buffer on the sample. This creates a gradient of the carrier protein in the background of the tracer gradient that may influence the diffusion of the tracer material through cross-term diffusion coefficients (Correia and Stafford 2015). We call these gradient method experiments (Fig. 1). It is also possible to layer carrier protein onto carrier protein plus tracer. This creates a constant background (Fig. 1, CB method) of carrier protein that allows for the measurement of the diffusion of the tracer in the absence of other gradients. The CB method is especially prone to convective mixing. It may be necessary to add 0.5–2% sucrose or some other stabilizer to the sample solution to minimize or prevent convection (Hersh and Schachman 1955; Vinograd et al. 1963).

Theory

These experiments allow for the determination of the nonideality that arises from the excluded volume and charge perturbation a macromolecule has on itself (self-term nonideality) or other components (cross-term nonideality). Equation 3 describes a two component macromolecular system where nonideality can be determined empirically through pair-wise specific experiments. In these studies the pair-wise experiments consist of any two of the following components: mAb (component 1), HSA (component 2), and IgG (component 3). The self-term nonideality is described by the k_{ii} or B_{ii} term where $i = i$ (Eqs. 3 and 5). For the cross-term nonideality, the term is denoted as k_{ij} or B_{ij} where $i \neq j$ (Eqs. 3 and 5). The sedimentation coefficient of the labeled species as a function of the unlabeled species determined

for pair-wise interactions for both the self- and cross-term nonideality can be expressed as

$$s_1 = \frac{s_1^0}{1 + k_{11}c_1 + k_{12}c_2} \tag{3}$$

For plotting purposes, the relationship can be simplified and rearranged into a linear equation due to the low concentration (100–200 nM) of the labeled component $k_{11}c_1$ which renders it negligible:

$$\frac{1}{s_1} = \frac{1}{s_1^0} + \frac{k_{12}}{s_1^0}c_2 \tag{4}$$

where the y-intercept is $1/s_1^0$ and the slope is the k_{12}/s_1^0 term. The slope gives the hydrodynamic nonideality exerted by the unlabeled component (in this case component 2 or HSA) on the labeled component (component 1 or mAb). The k_s (k_{12} in Eq. 4) value is determined by dividing the slope by the $1/s_1^o$ value.

The diffusion coefficient of the labeled species as a function of the unlabeled species determined for pair-wise interactions for both the self- and cross-term nonideality can be expressed as (Stafford and Sherwood 2004; Correia and Stafford 2015; Wright et al. 2018)

$$D_1 = \frac{D_1^0(1 + 2B_{11}M_1c_1 + 2B_{12}M_2c_2)}{(1 + k_{11}c_1 + k_{12}c_2)} \tag{5}$$

and then plotted as

$$D_1\left(1 + k_{12}c_2\right) = D_1^0(1 + 2B_{12}M_2c_2) \tag{6}$$

to determine the thermodynamic nonideality $2B_{12}M_2$ from the slope of the line. Note the B_{11} and k_{11} terms are eliminated because the labeled tracer concentration is low. The k_{12} or k_s values used were determined by sedimentation velocity experiments presented elsewhere (Wright et al. 2018). The experiments presented here test the ability of SB to accurately determine s and plots of s vs c to independently determine k_s values.

There are two general mathematical forms for concentration dependence of s: $s^o\ (1 - k^*c)$ and $s^o\ (1 + k_sc)^{-1}$. Throughout the text we will differentiate between the two plots by referring to k^* or k_s. A relationship between the two constants is derived in the discussion. The $(1 + k_sc)^{-1}$ form may be transformed into a $1/s$ vs c plot which is preferred because it is linear over a wider concentration range (Schachman 1959). The concentration used in a s vs c or a $1/s$ vs c plot from a traditional SV run must be corrected for radial dilution ($c^o/c = (r'/r_m)^2$) if s is determined by the program DCDT (Stafford 1992) or WDA (Stafford and Braswell 2004). The average position of the scans used in the analysis ($r' = r_m + (r - r_m)/2$) must be used to correct the average concentration, thus the average nonideality of the boundary is exposed during the run up to the time of analysis (Trautman and Schumaker 1954; Patel et al. 2018). This in principle also applies to synthetic boundary analysis and s or D vs c plots. However, we perform direct boundary SEDANAL fits that extract s and D values corresponding to the initial concentration. This is because Claverie (1976) solutions to the Lamm equation simulate the boundary position from time zero and thus correct for radial dilution. Since the SEDANAL fitting function is a single-component model, the results will be influenced by the presence of aggregated dimer or trimer species which are present in HSA and all IgG and mAb solutions. This is especially true at low speeds where the measured diffusion will reflect the distribution of species present and thus give an average s and D (see Fig. 9). Since the unlabeled carrier protein concentration is being plotted, we must also trust that the dilution factor for each optically invisible sample is correct. This may be in error if scattering artifacts alter the initial concentration determination, or if aggregates spin out of solution during the run and alter the actual concentration producing the nonideality.

Irreversible thermodynamics hypothesizes that coupled diffusion occurs in mixtures and serum solutions (Fujita 1975; Katchalsky and Curran 1975; Correia and Stafford 2015) as expressed in the modified Lamm equation shown below.

$$\sum\left(\frac{\partial c_i}{\partial t}\right)_r = -\sum\frac{\partial}{r\partial r}\left[c_i\omega^2 s_i r^2 - \sum_{j=1}^{n} D_{i,j}r\left(\frac{\mathrm{d}c_j}{\mathrm{d}r}\right)_t\right] \tag{7}$$

The summation terms over D_{ij} are derived from the coupled flow equation starting with the phenomenological equations that included Onsager's reciprocal relations $L_{ij} = L_{ji}$:

$$J_1 = -L_{11}\frac{\partial \mu_1}{\partial x} - L_{12}\frac{\partial \mu_2}{\partial x} \tag{8}$$

$$J_2 = -L_{21}\frac{\partial \mu_1}{\partial x} - L_{22}\frac{\partial \mu_2}{\partial x} \tag{9}$$

where J's are the flows, L's are Onsager cross coefficients, μ_i are chemical potentials and $\partial\mu_i/\partial x$ are the forces. Substituting for chemical potential and differentiating, thereby yields Fick's equation for two independent diffusional flows.

$$J_1 = -D_{11}\frac{c_1}{RT}\frac{\partial \mu_1}{\partial r} - D_{12}\frac{c_2}{RT}\frac{\partial \mu_2}{\partial r} \tag{10}$$

$$J_2 = -D_{21}\frac{c_1}{RT}\frac{\partial \mu_1}{\partial r} - D_{22}\frac{c_2}{RT}\frac{\partial \mu_2}{\partial r} \tag{11}$$

This equation shows that flow in a multicomponent system is coupled to total gradient of all components. Combining Eqs. 10 and 11 shows that $D_{12} \neq D_{21}$

$$D_{12} = L_{11}\frac{\partial \mu_1}{\partial c_2} + L_{12}\frac{\partial \mu_2}{\partial c_2} \tag{12}$$

$$D_{21} = L_{21}\frac{\partial \mu_1}{\partial c_1} + L_{22}\frac{\partial \mu_2}{\partial c_1} \tag{13}$$

The presence of coupled flow and cross-term diffusion coefficients is tested by comparing gradient and constant background experiments in pair-wise tracer experiments.

DLS

Measurements were performed on a DynaPro NanoStar instrument (Wyatt Technology) equipped with Dynamics V7 version 7.19 software. Samples (50–100 µl) were spun for 3 min at 20 °C and 50K rpm in a Beckman Optima TLX ultracentrifuge to avoid the presence of dust in the sample. Cells were loaded with 10 µl of sample directly from the centrifuge tube to avoid contaminating the sample with dust. The laser power was set at 50%. Measurements consisted of ten 5 s acquisition times that were averaged and repeated three times. The diffusion coefficient data were plotted vs concentration (mg/ml) as a mean ± SD of three repeats. The data were fit to the standard equation

$$D = D^{o}(1 + k_D c) \tag{14}$$

and k_D compared to $2BM$ values as determined above. k_D values are reported in units of ml/g. All results ($s^{o}_{20,w}$, k_s, k^*, $2BM$, k_D and $D^{o}_{20,w}$) are summarized in Table 1.

Results

A synthetic boundary centerpiece allows a buffer or protein solution to layon onto a protein solution to create a sharp boundary. Typical data are shown in Fig. 2 where Alexa-488-NIST mAb sediments and diffuses in 5 mg/ml unlabeled NIST mAb at (A) low and (B) high speed.

Analysis of these data was performed in SEDANAL with a modification of the Claverie (1976) algorithm that allows a sharp boundary or a band as an initial condition. Philo (1994) developed a synthetic boundary analysis option in his program SVEDBERG (newest version 7.0.7 that also works with FDS SB high speed data) and observed that the first few scans typically show convective optical imperfection and suggested using later scans for the initial scan in the fit. We observe the same effect and typically use scan 9 (~ 800 – 1200 s depending upon speed) to initialize the Claverie algorithm. The Svedberg equation

$$\frac{s}{D} = M(1 - v\rho)/\mathrm{RT} \tag{15}$$

contains three unknowns and only two of those are independent variables. Thus, SVEDBERG can fit for s and M, or D and M or s and D. Data for this study were typically fit to a single-species s and D model to extract both sedimentation and diffusion coefficients.

Table 1 Summary of the measured parameters

	$s^{o}_{20,w}$ (S)	k_s (ml/g)	k^* (ml/g)	2BM (ml/g)	k_D (ml/g)	$D^{o}_{20,w}$ (F)
HSA	4.61	3.3	2.9	5.1	4.5	5.47[a]
				3.0		5.50[b]
						5.30[c]
Fluorescein	0.21					42.13
NIST	6.99	− 1.4	− 1.4	0.3	− 2.5	3.95[d]
						4.06[e]
						4.00[c]
Golimumab	7.04	− 0.8	− 0.8	− 6.5	− 5.3	4.39[a]
				− 7.2		4.52[f]
						4.11[c]
NIST/HSA	7.21	7.1	5.6	3.2		4.17[d]
				2.6		4.19[e]
NIST/IgG	6.96	− 3.4	− 3.3	0.6		3.99[a]
	6.74	1.9	2.6	6.3		4.22[f]

[a]7K rpm
[b]35K rpm
[c]DLS
[d]Gradient
[e]CB
[f]24K rpm

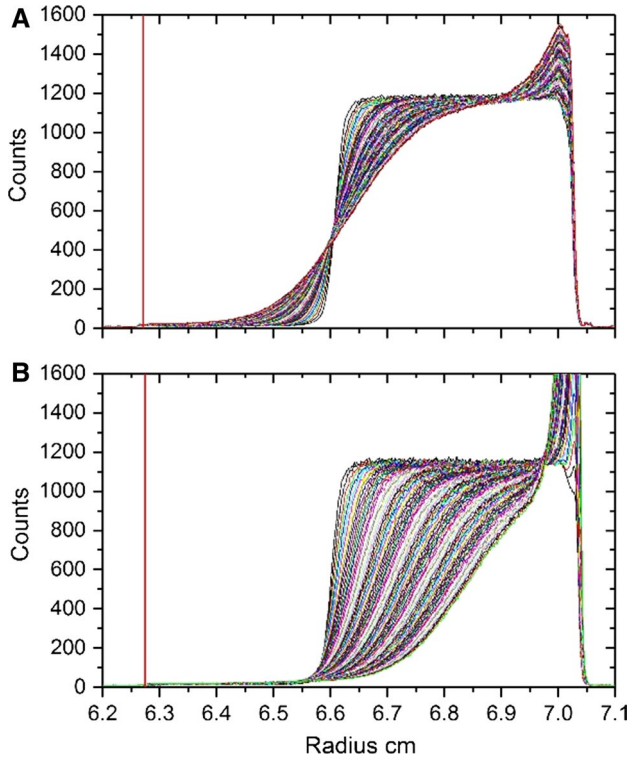

Fig. 2 Typical synthetic boundary data (100 scans) collected with the Aviv-FDS at **a** 7K rpm or **b** 24K rpm. Sample is 100 nM Alexa-488-NIST mAb in 5 mg/ml unlabeled IgG. The meniscus is indicated by the red line

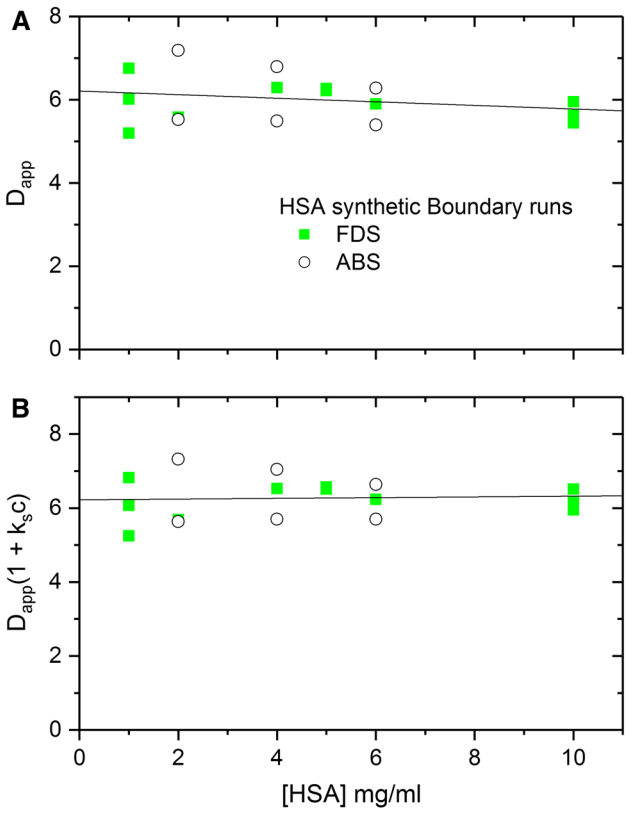

Fig. 3 Synthetic boundary diffusion coefficient data for unlabeled HSA (circles) by Abs and FITC-HSA by Aviv-FDS (squares). **a** D_{app} vs c plots and **b** $D_{app}(1+K_s{*}c)$ vs **c** D_{app} data are corrected with $(1+0.0094*c)$ from prior SV experiments (Wright et al. 2018). These data may be influenced by convective mixing, but most importantly by the influence of free FITC due to HSA reversible binding of small molecules

Synthetic boundary experiments with human serum albumin

HSA was our initial test system using both absorbance and FDS optics at both low (7K) and high (35K) speed (Fig. 3). BSA has been studied extensively and has a $D_{20,w}$ of 5.94 F, $s_{20,w}$ of 4.31 S, and 2BM of 3 ml/g (Tanford 1961) and HSA values are expected to be similar. Figure 3a shows that up to 10 mg/ml, D_{app} values determined from synthetic boundary experiments are scattered widely. The scatter results in a negative slope and a D^o value that is too large. Correcting the data for hydrodynamic nonideality $(1+k_s c)$ corrects the slope, but the data are still scattered. In addition, values of $2B_{22}M_2$ could not be determined reliably $(1.6 \pm 7.3$ ml/g). We believe that the problems may stem from the fact that the FITC-HSA tracer samples show evidence (raised baseline in SV runs) of non-covalently bound dye that was not removed by dialysis or spin-column buffer exchange. The dye slowly leaches from the HSA binding sites. Consequently, the diffusion data for HSA are too heterogeneous (Fig. 3) to provide reliable fitted values to a single-species model. However, data acquired using the absorbance optics also are scattered, suggesting that the problem may also arise from convective artifacts.

To test whether convection artifacts were the problem, we performed experiments with sucrose (1–5%; only the 1% data are presented here) included in the solution to density stabilize against convection. Furthermore, the data were analyzed using a two-species model to account for free label (Fig. 4). The correction for the additional viscosity (η) of 1% sucrose is small, $\eta_{T,b}/\eta_{20,w} \sim 2\%$.

The $s_{20,w}$ and $D_{20,w}(1+k_s c)$ data from FDS experiments conducted at 7K and 35K rpm, over a wide HSA concentration range (1–40 mg/ml), and including 1% sucrose are presented in Fig. 4. The raw data were fit to a two-species model with fluorescein s value fixed at 0.214 S (see experiments below) and D for fluorescein was allowed to float in the fit. The HSA sedimentation coefficient at 7K rpm is poorly determined. The boundary has minimal movement, with an intercept s^o of 4.60 ± 0.23 S, a positive slope and an average value of 4.65 ± 0.32 S. The sedimentation coefficient measured at 35K rpm is much better determined with an intercept s^o of 4.61 ± 0.15 S and a $k^*_{22} = 2.9 \pm 1.4$ ml/g ($k_{22} = 3.3 \pm 1.6$ ml/g). The k^*_{22} and

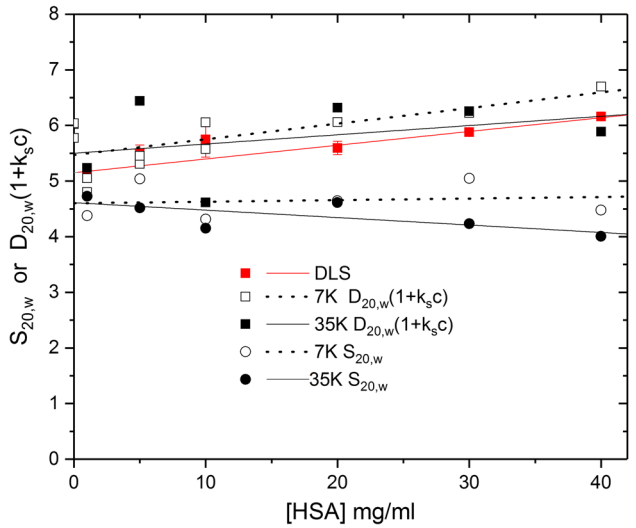

Fig. 4 Synthetic boundary $D_{20,w}$ and $s_{20,w}$ data on FITC-HSA +1% sucrose (viscosity corrected) at multiple speeds, 7K (open symbols) and 35K (solid symbols), plotted vs unlabeled carrier protein concentration. $D_{20,w}$ data are corrected with $(1+0.0094*c)$ from prior SV experiments (Wright et al. 2018). Also shown are DLS $D_{20,w}$ data (red squares) for HSA

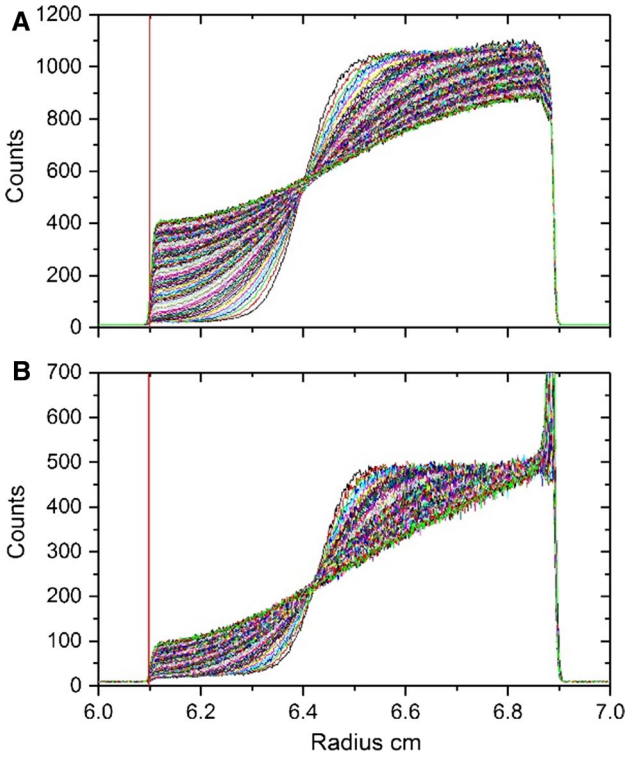

Fig. 5 SB FDS experiments (100 scans) with 150 nM fluorescein in **a** buffer at 7K rpm and **b** 1 mg/ml HSA at 50K rpm. The meniscus is indicated by the red line. Note, at 50k rpm a fraction of fluorescein pellets due to binding to HSA

k_{22} values determined here are small compared with values determined from SV experiments (Wright et al. 2018; see "Discussion"). The diffusion coefficient data at 7K give an intercept D^o of 5.47 ± 0.15 F (where $F = 1 \times 10^{-7}$ cm^2/s) with a positive $2B_{22}M_2 = 5.1 \pm 1.7$ ml/g. The 35K rpm data yield a D^o of 5.50 ± 0.50 F with a poorly determined $2B_{22}M_2$ of 3.0 ± 4.0 ml/g. The fitted value of D for fluorescein was 24.3 ± 6.2 F with a signal ratio F/HSA of 0.17 ± 0.08 at 35K rpm. Data obtained using DLS are shown on the same plot ($D_{20,w}$ vs c) and give a D^o of 5.30 ± 0.04 F and a $k_D = 4.5 \pm 0.3$ ml/g. Thus, adding sucrose and fitting with a two-species model improves the quality of the HSA synthetic boundary data and gives $2B_{22}M_2$ values that are very similar to those arising from DLS k_D measurements. All results are summarized in Table 1.

The s^o, D^o and $2B_{22}M_2$ values are similar to the values for BSA (Tanford, 1961) while k^*_{22} and k_{22} are significantly smaller, but similar to one another. There is more scatter in the SB $D_{20,w}$ data than in the DLS data, especially at low concentrations. The scatter in the SB data may arise from having to fit the additional parameters in the two-species model, or it might reflect the presence of convection. Furthermore, although we used a model that consists of two non-interacting species, the system actually contains reversibly interacting components (FITC + HSA↔ FITC-HSA), as well as the covalently bound FITC-HSA complex. Fitting synthetic boundary and band forming data with complex reversible binding models is currently under development in SEDANAL and will be presented elsewhere (see "Discussion").

Synthetic boundary experiments with fluorescein

To help interpret the FITC-HSA data (Fig. 4), SB experiments were performed on free fluorescein in the presence and absence of 1 mg/ml unlabeled HSA or IgG. This allows for separate measurement of the diffusion and sedimentation coefficient of fluorescein and the influence of these serum proteins on its diffusion (Fig. 5). At low speed there is no appreciable sedimentation (Fig. 5a), while at high speed a slight motion, indicated by the cross over point, is evident (Fig. 5b). The fluorescein sedimentation coefficient cannot be determined reliably from the 7K rpm data (0.448 ± 0.394 S), but at 50K rpm fluorescein s_{app} is reasonably well determined (0.214 ± 0.016 S; Table 1). It should be noted that the buoyancy term $(1-\nu\rho)$ was adjusted for fluorescein to 0.3727 so that s/D equaled the MW of fluorescein, ~ 332.31. For a measured buffer density of 1.00849 g/ml, the v_{bar} for fluorescein can be estimated to be 0.622 ml/g. At both speeds there is extensive diffusion back towards the meniscus, consistent with the small size of fluorescein. The

average measured $D_{20,w}$ for fluorescein is 40.78 ± 1.71 *F*, obtained from data acquired at both speeds with both FDS and absorbance optical systems. The $D_{20,w}$ value for fluorescein in 1 mg/ml HSA, 38.79 ± 0.55 *F*, is lower, but within the uncertainty of the protein-free value. Evidence of weak binding of fluorescein to HSA is revealed in Fig. 5b as: (a) the apparent pelleting of the dye and (b) the lower plateau concentration of the dye in the presence of HSA than in its absence (Fig. 5a). Dye binding by HSA may, in part, explain the large uncertainty in the HSA results (Fig. 3). In contrast, the average $D_{20,w}$ for fluorescein (± 1 mg/ml IgG) is 41.77 ± 0.98 *F* (see Table 1) which is in reasonable agreement with data obtained by FCS (42.5 ± 0.01; Kapusta 2010). The interpretation of data from mixtures of free label and label-binding proteins like HSA will require additional modeling, but the general impact on fitting is shown here. In the past, SB has been used to look at small peptides or proteins that do not form sharp boundaries in a standard sedimentation velocity run (Philo 1994; Schuck et al. 1998). To our knowledge there has been no systematic comparison of data acquired using Aviv-FDS SB and FCS. Since both methods are useful for measuring macromolecular diffusion coefficients in complex solutions, future comparisons might be informative (Sudhaharan et al. 2009).

NIST and golimumab mAb self-diffusion coefficients

A comparison using Alexa-488 labeled NIST mAb vs NIST mAb as the carrier protein in gradient and constant background (CB) mode is shown in Fig. 6. The data show no impact of the presence or absence of a gradient. Strictly this is a one-component system (ignoring the label on the tracer), so no difference is expected. There is scatter in the low concentration $D_{20,w}$ data, so CB data were gathered twice with 0.5% sucrose to verify reproducibility and the impact of a density stabilizer (open triangles). In general, sucrose improves the reproducibility and agrees with the trend of the other data. The $s_{20,w}$ data were fit jointly with s^o = 6.99 ± 0.07 S and poorly determined k_{11}* (− 1.4 ± 1.2 ml/g) and k_{11} (− 1.4 ± 1.2 ml/g) values. The negative k_{11}* and k_{11} values suggest weak association. Both the gradient and CB data give well-determined values of D^o (3.95 ± 0.02 F; 4.06 ± 0.10 F) and variable $2B_{11}M_1$ values (2.7 ± 0.5 ml/g; − 1.5 ± 3.4 ml/g). A joint fit to the data gives $2B_{11}M_1$ = 0.3 ± 2.2 ml/g. The DLS data are graphically in general agreement with D^o = 4.00 ± 0.02 F and k_D = − 2.5 ± 1.9 ml/g, and consistent with weak association. Taken together, nonideality data (k_{11}* and k_{11}, $2B_{11}M_1$ and k_D) for NIST mAb suggest a masking between hydrodynamic nonideality and self-association (Table 1; Wright et al. 2018). The apparent association is slightly larger than the nonideality, but reflects the presence of both effects. This result has encouraged us to directly measure the association constant, K_2, assuming dimerization, by global SEDANAL fitting of SV data over wider concentrations ranges, up to 120 mg/ml (Wright et al. 2018).

A comparison using Alexa-488 labeled golimumab mAb vs golimumab mAb as the carrier protein in gradient and CB mode is shown in Fig. 7. The gradient

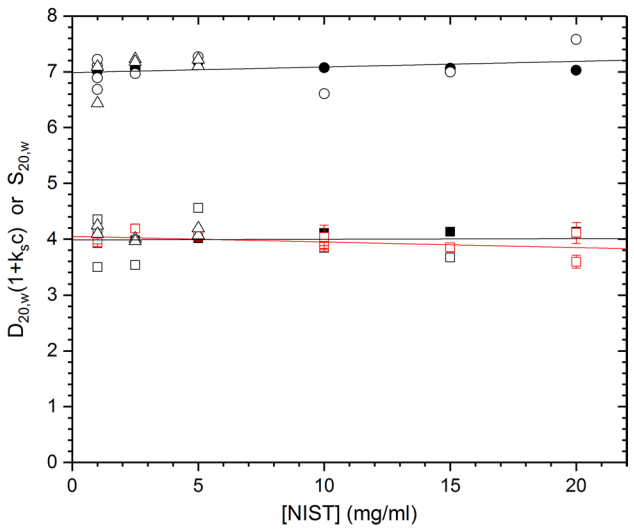

Fig. 6 Comparison of Alexa-488 NIST mAb vs NIST mAb in gradient (closed symbols) and CB (open symbols) mode at 7K rpm. Both $s_{20,w}$ (upper data) and $D_{20,w}$ (lower data) values are plotted. $D_{20,w}$ data are corrected with (1 + 0.0034 * *c*) from prior SV experiments (Wright et al. 2018). Also shown are DLS $D_{20,w}$ data (red squares) for NIST mAb. The 0.5% sucrose data are also corrected for sucrose viscosity (open triangles)

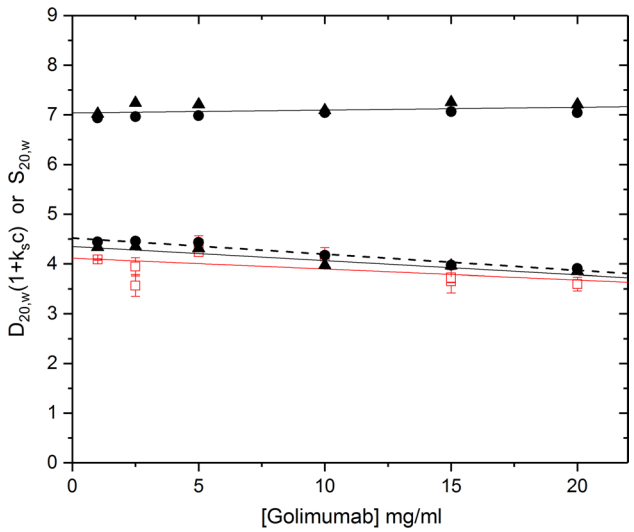

Fig. 7 Comparison of Alexa 488 golimumab mAb vs golimumab mAb in gradient (closed symbols) mode at 7K (squares) and 24K rpm (triangles). $D_{20,w}$ data were corrected with (1 + 0.0018 * *c*) from prior SV experiments (Wright et al. 2018). Also shown are DLS $D_{20,w}$ data (red squares) for golimumab mAb

experiment was repeated at 24K and gave similar results. The data are in general agreement with the presence of weak self-association. The diffusion data have similar intercepts ($D^o = 4.39 \pm 0.05$ F, 4.52 ± 0.04 F) and slopes ($2B_{11}M_1 = -6.5 \pm 1.1$ ml/g; -7.2 ± 1.1 ml/g) consistent with self-association. The DLS data are in general agreement with $D^o = 4.11 \pm 0.03$ and $k_D = -5.3 \pm 1.9$ ml/g and consistent with weak association. The $s_{20,w}$ data are also consistent with weak association although poorly determined k_{11}* and k_{11} values ($s^o = 7.04 \pm 0.05$ S; $k_{11}^* = -0.8 \pm 0.7$ ml/g; $k_{11} = -0.8 \pm 0.6$ ml/g). In general, the data suggest golimumab is a weakly associating mAb with a $D^o = 4.34 \pm 0.21$ F. The k_{11}, k^*_{11} and $2B_{11}M_1$ data are all consistent with association; however, no detailed association mechanism can be extracted from these graphical data. There is probably both nonideality and association occurring that masks one another's magnitude. Detailed direct boundary global fitting by SEDANAL of SV data at higher concentrations is required to extract K_2, k_{11} and $2B_{11}M_1$ separately (Hopkins et al. 2018; Wright et al. 2018; Yang et al. 2018).

NIST mAb cross-term effects with HSA

Figure 8 shows the results of Alexa-488-NIST run against HSA carrier protein in gradient and CB mode. Both the gradient and CB data give well-determined D^o (4.17 ± 0.03 F; 4.18 ± 0.06 F) and $2B_{12}M_2$ values (3.2 ± 0.3 ml/g; 2.6 ± 0.6 ml/g) that agree within error. There is no significant difference between the two modes, suggesting that cross-term diffusion coefficients are small under these conditions. The $s_{20,w}$ data were fitted jointly and gave $k^*_{12} = 5.6 \pm 0.2$ ml/g. A $1/s_{20,w}$ vs c plot gives a $k_{12} = 7.1 \pm 0.3$ ml/g which is very close to the value determined by SV (6.5 ml/g; Wright et al. 2018). The extrapolated s^o (7.21 ± 0.04 S) seems large and indicates the influence of aggregates. Both $2B_{12}M_2$ and k_{12} values are consistent with nonideality with no evidence of association between NIST and HSA. There also appears to be no free Alexa-488 present. These experiments were not repeated at 24K rpm because the NIST would sediment faster than the HSA and move away from the HSA gradient, thus negating the point of the experiment. This phenomenon is termed unmixing (see Wright, et al. 2018). Note further that a cross-term k_D effect cannot be measured by DLS because the carrier protein and not the NIST mAb would do all the scattering.

NIST mAb cross-term effects with IgG

Figure 9 shows Alexa-488 labeled NIST mAb runs against IgG as carrier protein in gradient and CB mode at 7K and 24K. There is no apparent cross-term diffusion coefficient as evidenced by the similarity of the data (see open and closed symbols and joint fits). There is an obvious speed dependence that may be due to the influence of aggregates or small oligomers on both s_{app} and D_{app} at low speed. At 7K rpm the D^o is 3.99 ± 0.04 F with a $2B_{13}M_3$ value of 0.6 ± 0.9 ml/g. At 24K rpm the D^o is 4.22 ± 0.12 F with a $2B_{13}M_3$ value is 6.3 ± 2.5 ml/g. The lower diffusion coefficient at 7K rpm could be due to aggregates or oligomers

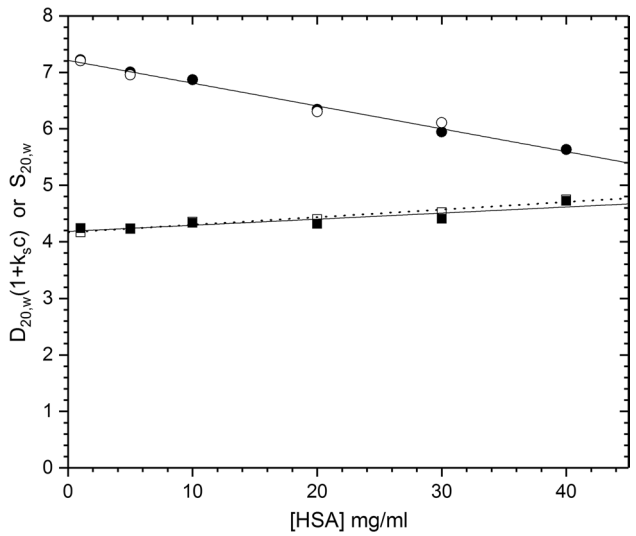

Fig. 8 150 nM Alexa-488 NIST with HSA carrier protein in gradient (closed symbols) and CB (open symbols) mode at 7K rpm in PBS without sucrose. Both $s_{20,w}$ (circles) and $D_{20,w}$ (squares) values are plotted. $D_{20,w}$ data were corrected with $(1 + 0.0065 * c)$ from prior SV experiments (Wright et al. 2018)

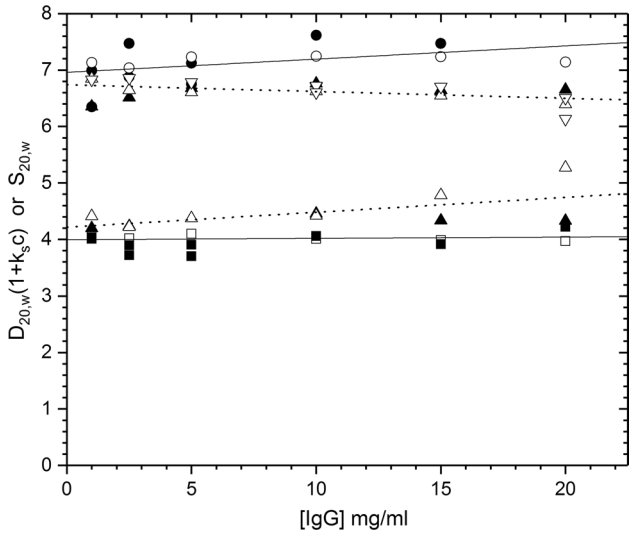

Fig. 9 150 nM Alexa-488 NIST with IgG carrier protein in gradient (solid symbols) and CB (open symbols) mode at 7K (solid lines) and 24K rpm (dotted lines) in PBS. Both $s_{20,w}$ (upper data) and $D_{20,w}$ (lower data) are plotted. $D_{20,w}$ data are corrected with $(1 + 0.0019 * c)$ from prior SV experiments (Wright et al. 2018). Gradient and CB data at each speed are jointly fit to estimate k_{13}* and $2B_{13}M_3$

not resolving and contributing to the single-component fit. The sedimentation data seem to support this assessment. At 7K rpm the s_{app} values are larger with $s^o = 6.96 \pm 0.12$ S and $k_{13}^* = -3.4 \pm 1.9$ ml/g ($k_{13} = -3.3 \pm 1.9$ ml/g). At 24K rpm the values are $s^o = 6.74 \pm 0.06$ S and $k_{13}^* = 2.6 \pm 1.4$ ml/g ($k_{13} = 1.9 \pm 0.7$ ml/g) and suggest aggregate resolving or pelleting and not contributing to the fit (see Table 1). Note this value of k_{13} is reasonably close to the value determined by SV (1.9 ml/g; Wright et al. 2018). The data suggest that heterogeneity due to aggregates or weak association can be a speed-dependent issue with these measurements. One way to explore this is to simulate heterogeneous and weakly interacting systems as a function of speed and then fit with various simple models. This will be a topic in our next manuscript on band sedimentation which seems to be more amenable to complex model fitting.

Both the NIST mAb in HSA and the NIST mAb in IgG datasets (Figs. 8, 9) suggest small cross-term diffusion coefficients (D_{12} or D_{13}). This is surprising since the irreversible thermodynamics of this is rigorous and well supported by theory (Fujita 1975; Katchalsky and Curran 1975; Correia and Stafford 2015). A different model system or much higher concentrations may be required to test this further. Most cross-term diffusion measurements have been done with salts or small molecules (Gosting 1956; Miller 1959). In one polymer example, Comper and Preston (1992) reported significant cross-term diffusion effects in an AUC SV ternary system involving dextran (T70 and T200 at 5, 10 and 20 mg/ml) and albumin (at concentrations of 50, 100 and 200 mg/ml). The experimental design produced concentration inversion and convective flow regimes. If inversions were observed in our experiments, the dataset was usually rejected.

Discussion

Synthetic boundary cells were first designed by Kegeles (1952) and separately by Pickles et al. (1952). They were utilized by numerous workers in the 1950s to study the basis for the concentration dependence of sedimentation (Kegeles and Gutter 1951; Schachman and Harrington 1954; Hersh and Schachman 1955, 1958). The approach, very similar to our CB method because they layer protein on protein plus an indicator, utilized Schlieren optics and created well-resolved peaks that then informed on self- and cross-term concentration dependence. The systems used included spherical (Bushy Stunt Virus, 130 s) and rod-shaped viruses (TMV, 170 s) that had large excluded or swollen volumes (Rowe, 1977, 1992) and thus very large back flow. In two sets of experiments, DNA and BSA actually moved backwards or with a negative sedimentation rate when run in the presence of BSV (Schachman and Harrington 1954; Hersh and Schachman 1958). To interpret these results Hersh and Schachman (1958) used the $(1 - k^*c)$ form of hydrodynamic nonideality since $(1 + k_s c)^{-1}$ does not generate negative sedimentation coefficients. The analysis incorporated a sum of terms for each component $(1 - k_1^* c_1 - k_2^* c_2 - \cdots)$ analogous to the $(1 + k_1 c_1 + k_2 c_2 + \cdots)^{-1}$ formulations used in SEDANAL (Stafford and Sherwood, 2004; Correia and Stafford 2015; Correia et al. 2016). At 10 mg/ml, TMV reduced the sedimentation coefficient of BSV by 64% which corresponds to a cross term k^* of ~ 33 ml/g; the BSV self k^* was ~ 9 ml/g. (These values are estimated directly from the figure in Harrington and Schachman (1953)). The original treatment of concentration dependence by Johnston and Ogston (1946) utilized $k(c_1 + c_2)$ or a global constant and total concentration. This approach was successful because the two components had similar $s(c)$. Subsequently Schachman proposed both backflow and viscosity as major sources of hydrodynamic nonideality (Harrington and Schachman 1953; Schachman 1959), although numerous factors including asymmetry, ionic strength and primary charge effect (Pederson 1958) were suggested as additional sources of concentration dependence. The AUC field began to focus on dilute solutions and concentration-dependent association reactions in the 1960s (Yphantis 1964). A primary use of synthetic boundary then became initial concentration measurements by interference optics for application to short-column sedimentation equilibrium methods to measure weight average molecular weights (Yphantis 1960; Correia and Yphantis 1992). Recently Philo and Maluf (2015) rediscovered this approach and applied it to the colloidal stability of protein pharmaceuticals.

Diffusion measurements were primarily performed with the Gosting diffusiometer in the 1950s (Baldwin et al. 1955; Dunlop and Gosting 1955; Gosting 1956). Measurement of D by synthetic boundary plot $(A/H_{max})^2$ vs time from Schlieren or interference optics (Svedberg and Pederson 1940; Fujita and MacCosham 1959; Stafford and Szent-Gyorgyi 1978; Philip et al. 1979) with a reported error of 6%. The method was considered to be extraordinarily difficult and not convenient for determination of molecular weight or shapes due in part to the poor dependence of D on size ($M^{-1/3}$; Cantor and Schimmel 1980). Convection from thermal fluctuations, vibrations, or density instability was a major concern (Hersh and Schachman 1955, 1958; Cantor and Schimmel 1980). Today, DLS and inelastic LS are considered the preferred methods for rapid and accurate determinations of diffusion properties. However, these methods work best on single, pure components and generally do not work with complex mixtures of macromolecules like serum. The Aviv-FDS SB method provides a unique opportunity to

study complex solution nonideality of mixtures, e.g., serum or cell extracts (Wright et al. 2018).

The DLS and AUC field has treated diffusion coefficient concentration dependence in a similar manner (Harding and Johnson 1985a, b). The relationship is

$$k_D = 2BM - k^*, \tag{16}$$

where the k^* term is derived from the Fujita approximation for sedimentation

$$s = s^o(1 - k^*c) \tag{17}$$

If k_s is determined from a $1/s$ vs c plot, then it is derived from the more linear form of the concentration dependence equation for s (Schachman 1959).

$$s = \frac{s^o}{(1 + k_s c)} \tag{18}$$

Dishon et al. (1967) showed 50 years ago that if it is assumed that

$$(1 - k^*c) = \frac{1}{(1 + k_s c)} \tag{19}$$

then by rearrangement

$$k^* = \frac{k_s}{(1 + k_s c)}, \tag{20}$$

which is a general expression that does not require assumptions about small kc values or any assumptions about the first term of a Taylor expansion. It is a useful expression when simulating concentration-dependent solutions to the Lamm equation. In general, our measurements suggest k^* and k_s are equivalent in estimating thermodynamic nonideality (Table 1) and agree with previous SV estimates (Correia et al. 2016; Wright et al. 2018) when association is not masking the nonideality effect (Figs. 8, 9).

A more general equation can be derived by assuming

$$(1 + k_D c) = \frac{(1 + 2BM_1 c)}{(1 + k_s c)} \tag{21}$$

and after similar rearrangement shows that

$$k_D = \frac{(2BM_1 - k_s)}{(1 + k_s c)}, \tag{22}$$

which is equivalent to the k^* expression above and also neglects any assumptions about small kc. It demonstrates that the DLS nonideality term k_D is both a hydrodynamic and a thermodynamic nonideality term derived from the concentration dependence of the frictional coefficient and the second virial coefficient, respectively.

Recent AUC transport studies have focused on orthogonal methods to measure hydrodynamic and thermodynamic nonideality coefficients (Solovyova et al. 2001; Saluja et al. 2010). These authors assume nonideality of the form given by Eq. (16). Crystallographers have used B to predict solution conditions that favor crystallographic propensity (George and Wilson 1994; Tessier and Lenhoff 2003). Solovyova et al. (2001), thus focused on solvent conditions that were useful for crystallography conditions for halophilic malate dehydrogenase. The magnitude of $2BM$ also depends upon preferential interactions of the protein with solvent components. Solovyova et al. (2001) have argued that sedimentation velocity experiments alone could be used to determine the concentration dependence of sedimentation, k^*, and diffusion, k_D. The requirements seem to be that the macromolecule is non-associating, and both k^* and k_D must be either positive or negative, where $k^* > k_D$, because the expression $2BM - k^*$ comprises terms of equal magnitude that almost cancel. Saluja et al. (2010) introduced the idea that k^* and k_D can have different signs that complicate the determination and evaluation of BM_1. Yadev et al. (2011, 2012) have described the use of second virial coefficient and k_D data in the development of therapeutic proteins. These nonideality indicators have been related to intermolecular interactions and predictors of protein precipitation, solubility and crystallization. As discussed above, negative $2BM$ and k_D values are consistent with molecular association and may be a means of screening and potentially rejecting candidates for future development. The pharmaceutical industry tends to use $2BM$ to predict what they call colloidal stability (Ahamed et al. 2007; Yadev et al. 2011, 2012). The presence of molecular association is generally considered something to be avoided.

The interpretation of k_D and k^* or k_s for associating systems becomes problematic (Rowe 2011; Wright et al. 2018). The problem is attractive interactions as reflected in a negative $2BM$ do not indicate the nature or strength of the interaction. To extract a mechanism with appropriate equilibrium constants, the data must be fit to a reversible interacting model. This is done most easily with sedimentation velocity or equilibrium methods (Solovyova et al. 2001; Rowe 2011; Wright et al. 2018). Since these data are usually collected at high concentration, repulsive interactions will be significant and must be added to the fitting model (including parameters K_2, k_s and $2BM$). This suggests that negative $2BM$, when measured by DLS or synthetic boundary methods described here, is a sum of effects that includes both repulsive and attractive interactions. This further explains the difficulty in assigning a meaning to a particular value of k_s, k_D or $2BM$. Nevertheless, much effort has gone into interpreting hydrodynamic nonideality for uncharged spheres and asymmetric macromolecules (Batchelor 1972; Rowe 1977, 1992; Harding and Johnson 1985a). More recent work is trying to parse the contributions, both the sign and the magnitude, of k_s

and $2BM$ to nonideality and reversible association (Wright et al. 2018; Yang et al. 2018).

The data collected here by synthetic boundary experiments and analyzed by $s_{20,w}$ and $D_{20,w}$ vs concentration plots are summarized in Table 1. Our data are in general agreement with the observations of previous workers. (Solovyova et al. 2001; Saluja et al. 2010). First, the magnitudes of k^*, k_s, BM_1 and k_D are quantitatively similar, and thus in typical difference formulations, $k_D = 2BM - k^*$, may cancel. For golimumab mAb an average $2BM - k^* = -6.8 - (-0.8) = -6.0$ which is close to the measured $k_D = -5.3$. Alternatively, for HSA an average $2BM - k^* = 4.0 - 3.1 = 0.9$ which essentially cancels and is not equal to $k_D = 4.5$. In addition for NIST mAb an average $2BM - k^* = 0.3 - (-1.4) = 1.7$ which has the opposite sign of $k_D = -2.5$. What is more evident in the data is that BM_1 and k_D are usually of the same magnitude as evident in the similar slope of all the DLS $D_{20,w}$ data and AUC data plotted as $D_{20,w}(1 + k_s c)$ (Figs. 4, 6, 7). Second, trends consistent with self-association are evident in all the parameters. This often means they have the same sign. NIST mAb has a negative k_s and k^*, a near-zero average $2BM$ and a negative k_D, all consistent with weak self-association. Golimumab mAb has negative k_s, k^*, $2BM$ and k_D values, which are also all consistent with weak self-association. Thus, evidence that mAb might not be good candidates for development as therapeutic antibodies is easy to get by multiple methods (Yadev et al. 2011, 2012). A factor not generally discussed by these authors is that self-associating mAbs will also exhibit nonideality, and the measurements indicate the relative strength of the association, but not the magnitude. A negative k_s and $2BM$ simply means a positive nonideal k_s and $2BM$ has been masked by a larger negative k_s and $2BM$ due to association. To fully dissect the contributions and determine both k_s and K_2 (if dimerization) requires more careful work (Rowe 2011; Wright et al. 2018). This usually means global fitting of SV data with a model that includes k_s, $2BM$ and an association constant K_2. We have recently discovered that experiments with mAb up to 120 mg/ml are capable of yielding k_s, $2BM$ and K_2, with the additional cost that higher order terms like $k'_s c^2$ must be included in the fitting above ~ 60 mg/ml. This means the plots are no longer linear and higher order terms are required.

The second virial coefficient B is a measurement of weak interactions between solutes. For pure solutes, Tanford derived equations for excluded volume effects for numerous shapes (Tanford 1961). Batchelor (1972) derived an expression for k_s for uncharged spheres, and Rowe (1977) derived an expression that includes a $(f/f_o)^3$ shape factor. Charge effects for $2BM$ are described by the Donnan effect which accounts for salt exclusion associated with macromolecular charge (Williams et al. 1958; Roark and Yphantis 1972). The value of B depends upon $(Z/M)^2$ divided by the salt concentration; therefore, high salt can suppress charge effects. The second virial coefficient of mAbs has traditionally been measured by static and dynamic light scattering methods. Sedimentation equilibrium is also a highly appropriate approach to measure B and higher order virial coefficients even in the presence of association (Roark and Yphantis 1972). However, there is no good theory for the impact of charge, pH or salt concentration on hydrodynamic nonideality (k_s) measurements (Moody and Shepard 2004). The nonideality will reflect the effective radius of the macromolecular Debye ion cloud (Onsager and Fuoss 1932; Fuoss 1959) and what Laue (2011) terms proximity energies. More importantly, salt may alter association reactions thus further complicating the interpretation. Additional experiments are needed to address these issues.

These are the first reported AU-FDS measurements by the SB technique. For our initial experiments, we compared absorbance and FDS optical methods for HSA and fluorescein and found reasonable consistency under low concentration conditions (Figs. 3, 5). We did not present data with IgG as a tracer because the initial absorbance data did not agree with the FDS data. There was a significant difference in D^o which suggested labeling was either altering the properties, or selectively labeling a subset of the total IgG fraction. This is a potential problem with FDS in general, that must be addressed for each molecular system studied. Nonetheless, in general the method gives reasonable indications of self- or cross-term nonideality or associating interactions. The signal-to-noise ratio for the FDS method is comparable to that for the absorbance system and exhibits similar statistics and reliability as measured by Fstat or bootstrap. The major issue with SB continues to be the tendency to exhibit convection even in the presence of low sucrose concentrations. In the absence of convective optical artifacts, the measurement of s and D is also sensitive to small amounts of aggregates present in HSA and mAb samples. At low speeds especially, s and D determinations by single-component models are average values that reflect the contributions from dimer, trimer and higher order aggregates. Higher speeds seem to improve this situation in some cases (Fig. 9). Parallel to these measurements, we have also performed band sedimentation studies (Vinograd et al. 1963; Dishon et al. 1969) and found less convection and improved resolution due to a longer sedimentation path. Aggregates and reversible interactions resolve more clearly during the later stages of the run allowing fitting with more complex models. We will present these results in a separate publication.

Conclusions

Methods are presented for performing synthetic boundary experiments to extract hydrodynamic k_s and thermodynamic $2BM$ nonideality parameters for the interaction of mAbs with serum proteins HSA and IgG. The method involves directly fitting Aviv AU-FDS synthetic boundary data with SEDANAL to extract $s_{20,w}$ and $D_{20,w}$ information. The data are then plotted vs carrier protein concentration to extract k^*, k_s and $2BM$ values. These graphical results reveal that mAbs may undergo weak self-association with negative nonideality parameters. The results are discussed in terms of future global direct boundary fitting methods that can be applied to resolve nonideality and weak association constants. This approach may be useful for a complete characterization of high concentration mAb formulations.

Acknowledgements Supported by Boehringer-Ingelheim and UMC AUC Facility. This work was presented at the 23rd International AUC Workshop and Symposium, Glasgow, Scotland. We thank Dave Bain, Tom Laue and Sharon Lobert for constructive comments.

Author contributions RTW and JJC designed and performed the experiments, analyzed and interpreted the data, and wrote the manuscript. WFS and PJS wrote the SEDANAL software modifications. DH provided materials and discussion. All authors did see and agreed to the final version of the manuscript.

Compliance with ethical standards

Conflict of interest The authors declare that they have no competing interests.

References

Ahamed T, Esteban BN, Thőmmes J (2007) Phase behavior of an intact monoclonal antibody. Biophys J 93:610–619

Baldwin RL, Dunlop PJ, Gosting LJ (1955) Interacting flows in liquid diffusion: equations for evaluation diffusion coefficients from moments of the refractive index gradient curves. JACS 77:5235–5238

Batchelor GK (1972) Sedimentation in a dilute dispersion of spheres. J Fluid Mech 52:245–268

Cantor CR, Schimmel PR (1980) Biophysical Chemistry, chapter 10-3. WH Freeman and Company, New York

Claverie JM (1976) Sedimentation of generalized systems of interacting particles. III Concentration-dependent sedimentation and extension to other transport methods. Biopolymers 15:843–857

Colfen H, Harding SE (1995) A study of Schieren patterns derived with the Beckman optima XL-A UV-absorbance optics. Prog Colloid Polym Sci 99:167–186

Comper WD, Preston BN (1992) The analytical ultracentrifuge as a tool for diffusion measurements. Cross diffusion effects in ternary polymer: polymer:solvent systems. In: Harding SE, Rose AJ, Horton JC (eds) Analytical ultracentrifugation in biochemistry and polymer sciences. Royal Society of Chemistry, pp 428–442

Correia JJ, Stafford WF (2015) Sedimentation velocity: a classical perspective. In: Coles J (ed) Methods in enzymology, vol 562. Academic Press, pp 49–80

Correia JJ, Yphantis DA (1992) Equilibrium sedimentation in short solution columns. In: Harding SE, Rowe AJ, Horton JC (eds) Analytical ultracentrifugation in biochemistry and polymer sciences. Royal Society of Chemistry, London, pp 231–252

Correia JJ, Lyons DF, Sherwood P, Stafford WF (2016) Techniques for Dissecting the Johnston-Ogston Effect. In: Uchiyama S, Arisaka F, Laue T, Stafford W (eds) Analytical ultracentrifugation—instrumentation, analysis and applications. Springer, Berlin, pp 243–262

Dhami R, Colfen H, Harding SE (1995) A comparative "Schlieren" study of the sedimentation behavior of three polysaccharides using the Beckman Optima XL-A and model E analytical ultracentrifuges. Prog Colloid Polym Sci 99:187–192

Dishon M, Weiss GH, Yphantis DA (1967) Numerical solutions of the LAMM equation. V. Velocity centrifugation. Biopolymers 5:697–713

Dishon M, Weiss GH, Yphantis DA (1969) Numerical solutions of the LAMM equation. V. Band centrifugation. Ann N Y Acad Sci 164:33–51

Dunlop PJ, Gosting LJ (1955) Interacting flows in liquid diffusion: expressions for solute concentration curves in free diffusion. JACS 77:5238–5249

Fujita H (1975) Foundations of ultracentrifugation analysis. Wiley, New York

Fujita H, MacCosham VJ (1959) Extension of sedimentation velocity theory to molecules of intermediate size. J Chem Phys 20:291–298

Fuoss RW (1959) The velocity field in electrolytic solutions. J Phys Chem 63:633–636

George A, Wilson WW (1994) Predicting protein crystallization from a dilute solution property. Acta Crystallogr D Biol Crystallogr 50:361–365

Gosting LJ (1956) Measurement and interpretation of diffusion coefficients of proteins. Adv Protein Chem 11:429–554

Harding SE, Johnson P (1985a) The concentration dependence of macromolecular parameters. Biochem J 231:543–547

Harding SE, Johnson P (1985b) Physicochemical studies on turnip-yellow-mosaic virus: homogeneity, relative molecular masses, hydrodynamic radii and concentration-dependence of parameters in non-dissociating solvents. Biochem J 231:549–555

Harrington WF, Schachman HK (1953) Analysis of a concentration anomaly in the ultracentrifugation of mixtures. JACS 75:3533–3539

Hayes DB, Philo JP, Laue TM (1994) Sednterp: interpretation of sedimentation data version 1.x. 2000 lines of visual basic code, written for Windows 3.x

Hersh RT, Schachman HK (1955) Ultracentrifugation studies with a synthetic boundary cell. II. Differential sedimentation. J Am Chem Soc 77:5228–5534

Hersh RT, Schachman HK (1958) Ultracentrifugation studies with a synthetic boundary cell. III. Sedimentation of a slow component in the presence of a faster species. J Phys Chem 62:170–178

Hopkins MM, Lambert CM, Bee, JS, Parupudi A, Bain DL (2018) Determination of interaction parameters for reversibly self-associating antibodies: a comparative analysis. J Pharm Sci 107:1820–1830

Johnston JP, Ogston AG (1946) A boundary anomaly found in the ultracentrifugal sedimentation of mixtures. Trans Faraday Soc 42:789–799

Kapusta P (2010) PicoQuant GmbH application note: absolute diffusion coefficients: compilation of reference data for FCS calibration

Katchalsky A, Curran PF (1975) Nonequilibrium thermodynamics in biophysics. Harvard University Press, Cambridge

Kegeles G (1952) A boundary forming technique for the ultracentrifuge. JACS 74:5532–5534
Kegeles G, Gutter FJ (1951) The determination of sedimentation constants from Fresnel diffraction patterns. JACS 73:3770–3777
Kroe RR, Laue TM (2009) NUTS and BOLTS: applications of fluorescence-detected sedimentation. Anal Biochem 390:1–13
Laue TM (2011) Proximity energies: a framework for understanding concentrated solutions. J Mol Recognit 25:165–173
Laue TM, Shah BD, Ridgeway TM, Pelletier SL (1992) Computer-Aided Interpretation of analytical sedimentation data for proteins. In: Harding SE, Rose AJ, Horton JC (eds) Analytical ultracentrifugation in biochemistry and polymer sciences. Royal Society of Chemistry, pp 90–125
Lyons DF, Lary JW, Husain B, Correia JJ, Cole JL (2013) Are fluorescence-detected sedimentation velocity data reliable? Anal Biochem 437(2):133–137
MacGregor IK, Anderson AL, Laue TM (2004) Fluorescence detection for the XLI analytical ultracentrifuge. Biophys Chem 108:165–185
Miller DG (1959) Thermodynamics of irreversible processes. The experimental verification of the Onsager reciprocal relations. Chem Rev 60:15–37
Moody TP, Shepard HK (2004) Nonequilibrium thermodynamics of membrane-confinement electrophoresis. Biophys Chem 108:51–76
Onsager L, Fuoss RW (1932) Irreversible processes in electrolytes diffusion, conductance, and viscous flow in arbitrary mixtures of strong electrolytes. J Phys Chem 36:2689–2778
Patel TR, Winzor DJ, Scott DJ (2018) Allowance for radial dilution in evaluating the concentration dependence of sedimentation coefficients for globular proteins. Eur Biophys J 47:291–295
Pederson KO (1958) On charge and specific ion effects on sedimentation in the ultracentrifuge. J Phy Chem 62:1282–1290
Philip M, Jamaluddin M, Venkata Rama Sastry R, Sharay Chandra H (1979) Nucleosome core histone complex isolated gently and rapidly in 2 M NaCl is octameric. PNAS 76:5178–5182
Philo JS (1994) Measuring sedimentation, diffusion and molecular weights of small molecules by direct fitting of sedimentation velocity concentration profiles. In: Schuster TM, Laue TM (eds) Modern analytical ultracentrifugation, Birkhauser, pp 156–170
Philo J, Maluf NK (2015) New approaches to investigating the self-association and colloidal stability of protein pharmaceuticals at high concentration, HOS 2015. https://www.slideshare.net/kbibiopharma/new-approaches-to-investigating-the-selfassociation-and-colloidal-stability-of-protein-pharmaceuticals-at-high-concentrations. Accessed 11 July 2018
Pickles EG, Harrington WF, Schachman HK (1952) An ultracentrifuge cell for producing boundaries synthetically by a layering technique. PNAS 38:943–9948
Roark DE, Yphantis DA (1972) Equilibrium centrifugation of nonideal systems. The Donnan effect in self-associating systems. Biochemistry 10:3241–3249
Rowe AJ (1977) The concentration dependence of transport processes: a general description applicable to sedimentation, translational diffusion, and viscosity coefficients of macromolecular solutes. Biopolymers 16:2595–2611
Rowe AJ (1992) The concentration dependence of sedimentation. In: Harding SE, Rowe AJ, Horton JC (eds) Analytical ultracentrifugation in biochemistry and polymer science. Royal Society of Chemistry, Cambridge, pp 394–406
Rowe AJ (2011) Ultra-weak reversible protein–protein interactions. Methods 54:157–166
Saluja A, Fesinmeyer RM, Brems DN, Gokarn YR (2010) Diffusion and sedimentation interaction parameters for measuring the second virial coefficient and their utility as predictors of protein aggregation. Biophys J 99:2657–2665
Schachman HK (1959) Ultracentrifugation in biochemistry. Academic Press, New York
Schachman HK, Harrington WF (1954) Ultracentrifugation studies with a synthetic boundary cell. I. General applications. J Polymer Sci. 12:379–390
Schuck P, MacPhee CE, Howlett GJ (1998) Determination of sedimentation coefficients for small molecules. Biophy J 74:466–474
Solovyova A, Schuck P, Costenaro L, Ebel C (2001) Non-ideality by sedimentation velocity of halophilic malate dehydrogenase in complex solvents. Biophys J 81:1868–1880
Stafford WF (1992) Boundary analysis in sedimentation transport experiments: a procedure for obtaining sedimentation coefficient distributions using the time derivative of the concentration profiles. Anal Biochem 203:295–301
Stafford WF, Braswell EH (2004) Sedimentation velocity, multi-speed method for analyzing polydisperse solutions. Biophys Chem 108:273–279
Stafford WF, Sherwood PJ (2004) Analysis of heterologous interacting systems by sedimentation velocity: curve fitting algorithms for estimation of sedimentation coefficients, equilibrium and kinetic constants. Biophys Chem 108:231–243
Stafford WF, Szent-Gyorgyi AG (1978) Physical characterization of myosin light chains. Biochemistry 17:607–614
Sudhaharan T, Liu P, Foo YH, Bu W, Lim KB, Wohland T, Ahmed S (2009) Determination of in vivo dissociation constant, *KD*, of Cdc42-effector complexes in live mammalian cells using single wavelength fluorescence cross-correlation spectroscopy. JBC 284:13602–13609
Svedberg T, Pederson KO (1940) The ultracentrifuge. Oxford Press, London
Tanford C (1961) Physical chemistry of macromolecules. Wiley, New York
Tessier PM, Lenhoff AM (2003) Measurements of protein self association as a guide to crystallization. Curr Opin Biotechnol 14:512–516
Trautman R, Schumaker V (1954) Generalization of the radial dilution square law in ultracentrifugation. J Chem Phys 22:551–554
Vinograd J, Bruner R, Kent R, Weigle J (1963) Band-centrifugation of macromolecules and viruses in self-generating density gradients. PNAS 49:902–910
Williams JW, vanHolde KE, Baldwin RL, Fujita H (1958) The theory of sedimentation analysis. Chem Rev 58:715–806
Wright RT, Hayes DB, Stafford WF, Sherwood PJ, Correia JJ (2018) Pre-clinical biophysical characterization of therapeutic antibodies in human serum by analytical ultracentrifugation. Anal Biochem 550:72–83
Yadav S, Scherer TM, Shire SJ, Kalonia DS (2011) Use of dynamic light scattering to determine second virial coefficient in a semidilute concentration regime. Anal Biochem 411:292–296
Yadav S, Scherer TM, Shire SJ, Kalonia DS (2012) Viscosity behavior of high-concentration monoclonal antibody solutions: correlation with interaction parameter and electroviscous effects. J Pharm Sci 101:998–1011
Yang D, Correia JJ, Stafford WF, Roberts CJ, Singh S, Hayes D, Kroe-Barrett R, Nixon A, Laue TM (2018) Weak IgG self- and hetero-association characterized by fluorescence analytical ultracentrifugation. J Protein Sci 27:1334–1348
Yphantis DA (1960) Rapid determination of molecular weights of peptides and proteins. ANYAS 88:586–601
Yphantis DA (1964) Equilibrium ultracentrifugation of dilute solutions. Biochemistry 3:297–317